UNIVERSITI MALAYSIA PERLIS
International Journal of Nanoelectronics and Materials
IJNeaM
ISSN 1985-5761 | E-ISSN 2232-1535

Creep Rupture and Thermal Shock Failures of Nickel-based Alloy Reformer Tubes: A Comparative Analysis

Nur Farhana Hayazi*, Junaidi Che Halim and Ku Adri Azhan Ku Mohamad

Surface Technology Special Interest Group, Faculty of Chemical Engineering and Technology, Universiti Malaysia Perlis (UniMAP), Arau, Perlis, Malaysia
**Corresponding author. Tel.: +604-9798751; fax: +604-9798755; e-mail: farhanahayazi@unimap.edu.my*

ABSTRACT

This paper examines the failures of radiant tubes within a fertilizer plant's steam reforming unit between the creep rupture and thermal shock, encompassing discussions on the characteristics of the failures, microstructural analysis of the failures, the mechanisms of degradation at high temperatures, and forthcoming preventive actions. The primary reformer is where the initial stage of the steam reforming process occurs, involving the downward passage of a preheated hydrocarbon and steam mixture through radiant tubes containing catalysts. The resulting reformed gas, enriched with carbon monoxide, is further processed into ammonia- rich synthesis gas. These radiant tubes, crafted through centrifugal casting and primarily composed of 35% nickel and 25% chromium, operate at temperatures of 910^{0}C. The discovery of a leaking radiant tube necessitated an unscheduled shutdown, with the failure manifesting as an elliptical window-shaped rupture situated 590 mm from the tube's upper end. The affected tube was subsequently removed, and the outlet weldolet was sealed. During an online refractory repair operation, a catalyst tube exhibited a circumferential crack at a location 770 mm from the tube's upper end. At the same time, another catalyst tube was also observed with a longitudinal crack located at 5130 mm from the tube's upper end. To address these issues, both tubes were isolated from service through crimping at the top inlet hairpin and bottom outlet pigtail. Detailed metallurgical and failure analyses unveiled that one of the failures was initiated by intergranular cracking at the outer diameter, associated with thermal shock-induced cracking, followed by fatigue-driven crack propagation due to thermal stress and cyclic loading. Meanwhile, the other failed tube identified creep as the failure mechanism due to a combination of time, temperature and stress under such extreme operating conditions. The paper further explores the similarities and differences between these two radiant tube failure incidents and associated failure morphology and mechanisms.

Keywords: *Primary reformer, Creep rupture, Intergranular crack, Thermal shock, Failure analysis, Steam reforming*

1. INTRODUCTION

The failure analysis of steam-reforming radiant tubes is a vital investigation as radiant tubes are critical components in the primary reformer of ammonia production plants. The primary reformer initiates the steam reforming process, a key step in producing ammonia-rich synthesis gas. These tubes are exposed to extreme operating conditions, enduring temperatures as high as 910^{0}C [1, 2]. Understanding the causes of radiant tube failures is crucial in maintaining the stability of ammonia production facilities. Such failures may encompass a range of issues, including corrosion, thermal fatigue, and high-temperature degradation mechanisms [3, 4]. To shed light on these complexities, this paper embarks on an in-depth exploration of two specific failure observations; creep rupture and thermal shock failures.

The choice of catalyst is critical, as it influences reaction rates and product quality. The catalyst tube's design and material composition must withstand extreme operating conditions, including thermal stress and pressure, making it a key component in the efficient and reliable operation of a steam reforming unit. In the steam reforming process, the careful control of temperature within the catalyst tube from the top part to the bottom part is of paramount importance to ensure the success of the chemical reactions taking place. The catalyst tube is designed to have a deliberate temperature gradient from the outer surface to the innercore. At the top part of the tube, where the feedstock mixture is introduced, temperatures are relatively cooler, typically influenced by external factors such as the radiant heat from burner flames and other available heat sources. As the reactants progress downwards through the tube, they are subjected to increasing levels of heat. This temperature gradient is essential for staged reaction kinetics, allowing chemical transformations to occur in a controlled manner. By the time the reactants reach the lower section of the tube, they are exposed to the highest temperatures required for efficient reforming reactions.

The outer temperature of the tube is influenced by factors like burner settings, external insulation, and the surrounding environment. Conversely, the inner part of the tube, housing the catalyst bed, must achieve and maintain the specific, elevated temperatures needed for the reforming reactions to proceed effectively. This delicate balance in temperature distribution is achieved by careful engineering of the tube's material properties and insulation, as well as precise control of the combustion process. The temperature gradient, from the outer surface to the inner core, ensures that the catalyst is exposed to the ideal thermal conditions to facilitate the chemical reactions, ultimately leading to the production of hydrogen and carbon monoxide, key components in various industrial processes.

The first observation involved the unexpected leakage of one radiant tube, necessitating an unplanned shutdown after the tube had been in service for approximately 6 years. This incident was marked by an elliptical window-shaped rupture situated 590 mm from the top of the tube. The immediate response involved the removal of the failed tube and plugging the outlet weldolet. The second and third tube failures were discovered almost concurrently during an unplanned online refractory repair 7 years after the first incident. The second tube brought to light a circumferential crack while the third tube revealed a longitudinal crack at a distance of 770 mm and 5130 mm from the tube's top respectively. Subsequent analysis uncovered that intergranular crack initiation on the tube's outer diameter was a critical factor, associated with thermal shock cracking, followed by crack propagation fueled by fatigue mechanisms due to thermal stress and cyclic loading [2].

The predominant damage mechanism in reformer tubes revolves around the interplay between thermal stresses and internal pressure stresses [5]. Thus, the combination of these stresses causes creep damage to develop on the inside diameter. What makes this damage mechanism particularly challenging is the combined effect between these stresses; temperature fluctuations can influence pressure stresses, and vice versa. When these two stressors coincide and interact, they can significantly accelerate material degradation, leading to fatigue, cracking, and, in severe cases, catastrophic failure. Effective mitigation strategies, including appropriate material selection, sound design, and robust maintenance practices, are crucial to ensure the extended lifespan, safety, and reliability of reformer tubes in industrial applications.

This paper focuses on a comparative analysis of creep rupture and thermal shock failures in nickel-based alloy reformer tubes by examining the morphology of these radiant tube failures, analysing their microstructures, and investigating the high-temperature degradation mechanisms. By understanding the similarities and differences between these failure modes, the study aims to identify the primary causes of failure, offering valuable insights for developing preventive strategies and guiding future research to improve the reliability of radiant tubes in steam-reforming processes.

2. METHODOLOGY

A failure analysis was conducted on two cut-out leaked radiant tubes, marked and identified as tubes A and B from the primary reformer failure incidents after 122640 hours (14 years) of service. Chemical analysis was conducted on the base metal of tubes A and B in accordance with ASTM E415-17 [6]. A visual and macroscopic examination accompanied by photographic documentation was performed on the received cut-out sections of the radiant tubes. Fractographic examination was conducted on the fracture surface of the two cut-out tubes using a Hitachi SU1510 scanning electron microscope (SEM). The fracture surface was ultrasonically cleaned in Alconox solution prior to SEM examination.

Semi-quantitative EDX analysis was conducted on the fracture surface, inner diameter (ID) surface, outer diameter (OD) surface and base metal of tubes A and B using an EDX analyzer coupled to the Hitachi SU1510 SEM. The EDX results are summarised and compiled. Sectional metallographic examination was conducted transversely across the following locations of the two cut-out tubes. The selected sections were mounted, ground, polished and etched in accordance with ASTM E3-11 (Ra 2017) [7] and ASTM E407-07 (Ra 2015) [8] to reveal the microstructure and microscopic features. The Vickers micro-hardness test was performed on the examined representative metallographic sections using an Akashi MVK-G1 hardness tester at 55X magnification with a penetration load of 300gf. The test was carried out in accordance with ASTM E384-22 standard [9].

Lastly, tensile testing was conducted along the longitudinal axis of the two cut-out tubes according to ASTM E8/E8M-22 [10]. The tensile strength of both tubes generally complied with the tensile requirements of H39WM alloy steel material, which required a minimum strength of 450 N/mm^2. Characteristics of both tubes were later discussed and compared.

3. RESULTS AND DISCUSSION

The physical conditions and laboratory results of the two cut-out tube sections received are discussed. A longitudinal crack was found 5180 mm away from the top edge of tube A, while a circumferential crack was found 770 mm away from the top edge of tube B, right below the insulation area of tube B. The service parameters of the tubes are tabulated in Table 1.

Table 1 Service parameters of both tubes

Parameter	Specification
Service Medium	Methane gas
Operating Pressure	3.92 MPa
Design Temperature	910^{0}C
Operating Temperature	895^{0}C (as stated in the drawing)

The tubes were reportedly constructed of H39WM (Nickel-based) alloy steel, with an ID of 126.8 mm and an OD of 152.0 mm and a minimum required thickness of 11.8 mm.

3.1 Chemical Composition Analysis

Chemical composition analysis was conducted on the base metal of tubes A and B in accordance with ASTM E415- 17 [6]. The chemical composition results of the two cut-out tubes are tabulated in Table 2. The chemical composition of the tubes generally complied with H39WM heat-resistant cast alloy steel material specification, apart from the marginally higher silicon contents than the specified maximum limit. It was noted that a high silicon content will facilitate the formation of intermetallic niobium-nickel silicides, which will decrease the creep resistance of the cast material. Nevertheless, the marginally higher silicon content in both tubes had not likely affected the creep resistance of the tubes significantly especially in view that the tubes had been in service for over 14 years.

Nickel element in this material improves the hardness and strength properties without decreasing ductility and toughness, in contrast to chromium and carbon. Chromium, on the other hand, enhances steel's heat treatment, increasing both its strength and hardness while maintaining strength at elevated temperatures, resulting in improved resistance to corrosion and abrasion. Consequently, niobium plays a role in stabilizing carbon through the formation of hard carbides, making it a common component in high-temperature steels. In small amounts, niobium significantly boosts the yield strength and, to a lesser extent, the tensile strength of steels, also offering a moderate precipitation-strengthening effect.

Table 2 Chemical composition results of the two cut-out tubes A and B

Tube		A	B	H39WM Requirement [11]
Elemental Composition (wt%)	C	0.400	0.370	0.35-0.45
	P	0.010	0.011	0.03 max
	S	0.006	0.008	0.03 max
	Mn	1.000	0.920	1.5 max
	Si	2.220	2.160	1.5-2.0
	Cr	25.200	25.500	23.0-27.0
	Mo	0.038	0.061	0.5 max
	Ni	33.800	33.400	33.0-37.0
	Nb	1.090	1.000	0.7-1.5

3.2 Visual and Macroscopic Examination

The received cut-out sections of the radiant tubes were examined visually and macroscopically accompanied by photographic documentation. Figures 1 to 9 present general and close-up views of the examined samples, A and B. Figures 1 and 2 show the general views of the as-received tube A and the outside diameter surface respectively. The cut-out tube was around 1300 mm long. The longitudinal rupture crack was 140 mm long, with a slight bulge at the crack mouth. Apart from the crack and fissures, the OD surface was generally intact revealing a darkish appearance. The crack had a jagged appearance (Figure 2) with fissures. The fissures were intermittent in nature and extended over a length of around 130 mm towards the top of the ruptured crack. The cracks and fissures were oriented along the same axis on one side of the tube circumference.

Figures 3 and 4 show tube A's internal surface and fracture images. The tube was sectioned into two longitudinal halves to examine the ID surface. The ID surface was generally intact with no significant wastage or deposition apart from the rupture crack as shown in Figure 3. The rupture crack was later sectioned at its two ends to open for examination of the mating fracture surfaces (Figure 4). The fracture surface was greyish in appearance with scattered presence of adherent greenish scales or deposits. Grainy features were observed adjacent to the ID surface and extended transversely up to one-fourth of the wall thickness. The rest of the fracture surface revealed undulating ridge-like features which were oriented transversely across the tube wall.

Figures 5 and 6 show the general views of the as- received tube B and the external surface respectively. The cut-out tube was 380 mm long. An approximately 260 mm long circumferential U-shaped crack was observed propagating transversely across up to two-thirds of the tube OD (Figure 5). The OD surface of the tube had a brownish appearance towards the upstream side of the fracture, which was likely associated with the insulation layer. The OD surface downstream of the fracture revealed a more darkish appearance. The crack appeared to follow a generally straight path between the two crack ends and became more jagged towards the two crack ends as shown in Figure 6.

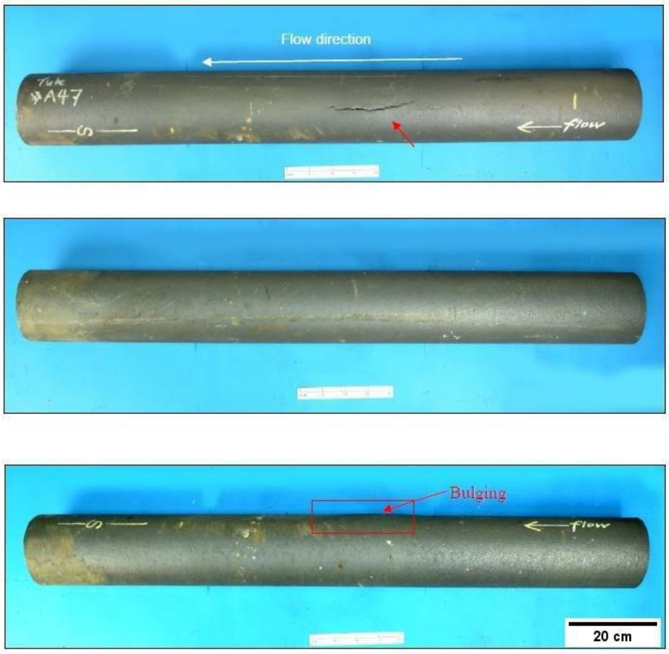

Figure 1. General Views of As-Received Tube A.

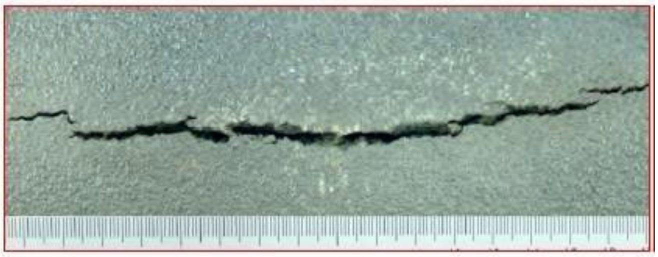

Close up view of rupture

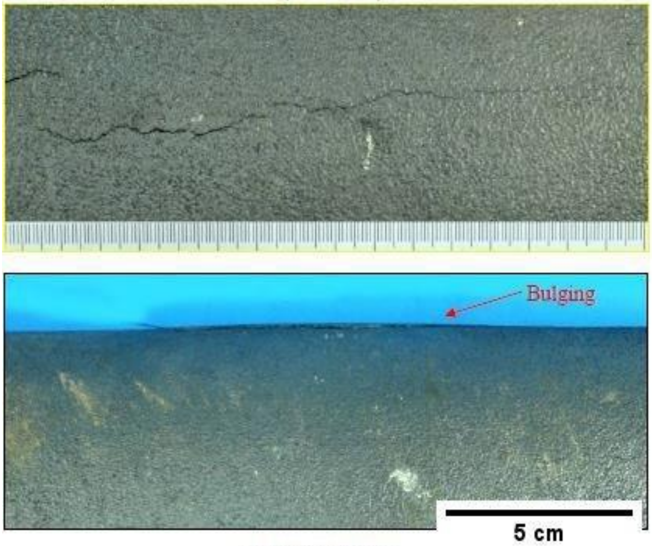

Side view of rupture

Figure 2. General Views of Tube A – OD Surface for both close-up and side views.

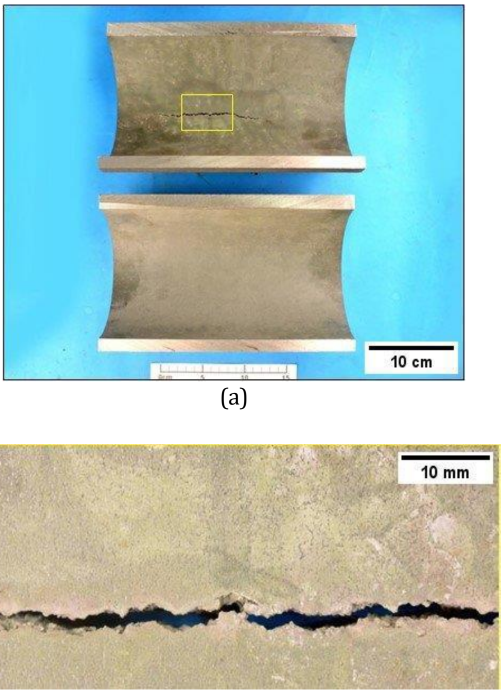

(a)

(b)

Figure 3. Tube A— ID Surface. The ID surface was generally intact apart from the rupture crack.

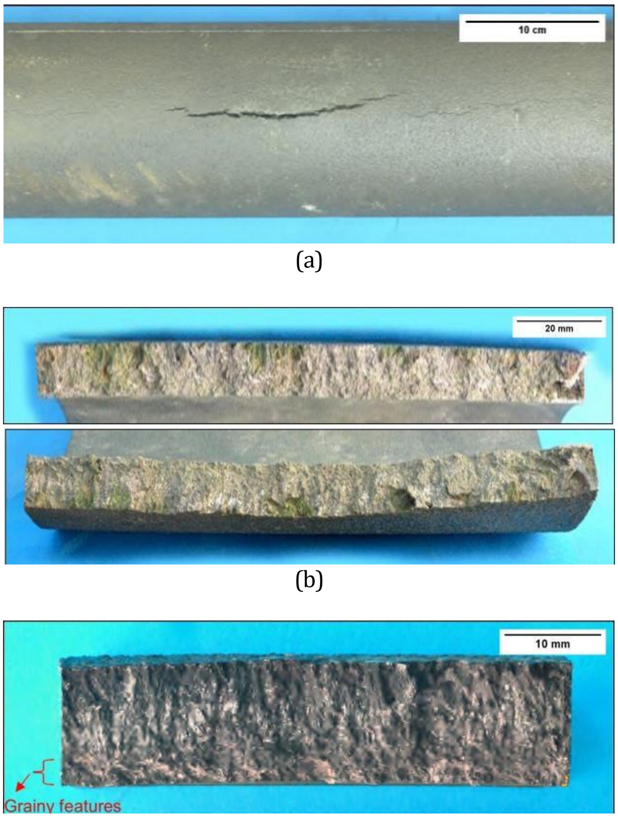

(a)

(b)

(c)

Figure 4. Tube A－Fracture Surfaces (a) overall view, (b) before cleaning and (c) after cleaning.

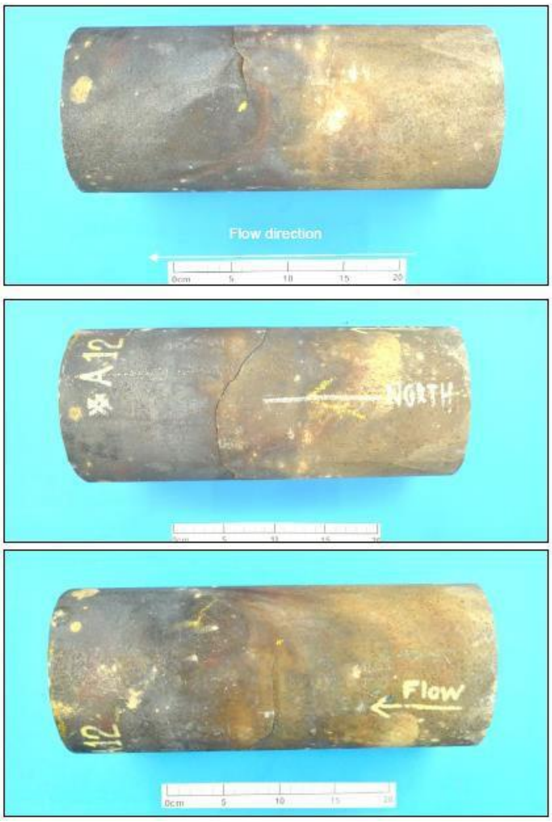

Figure 5. General Views of As-Received Tube B.

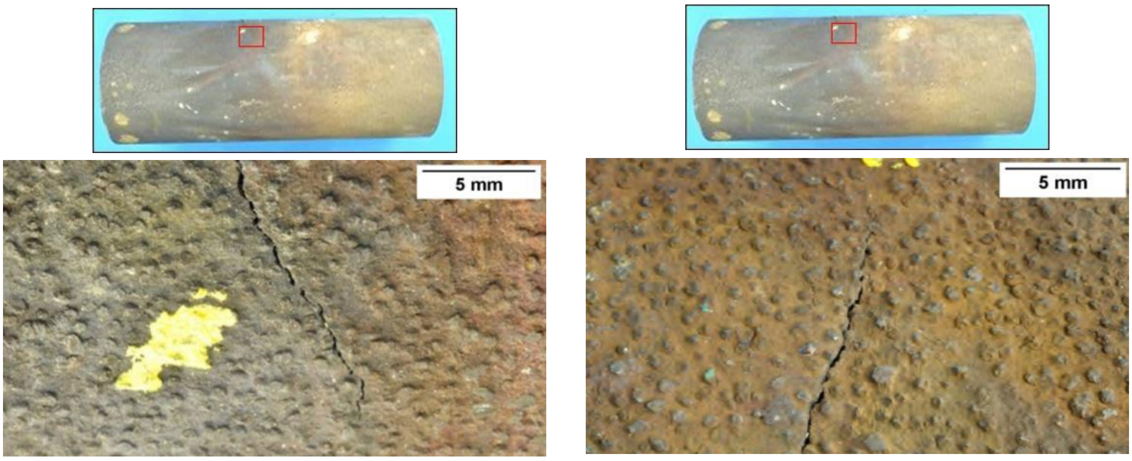

(a) (b)

Figure 6. Tube B – OD Surface.

Figures 7 and 8 show tube B's internal surface and fracture images. The tube was sectioned into two longitudinal halves to examine the ID surface. The ID surface was generally intact with no significant wastage or deposition apart from the rupture crack. The circumferential crack was later sectioned at its two ends to open for examination of the mating fracture surfaces (Figure 8). The fracture surface was generally covered with adherent darkish scales or deposits. A couple of relatively flat thumbnail regions, suggesting the initiation sites of the crack, were observed adjacent to the OD of the tube. Undulating ridge-like features were observed emanating from the thumbnail regions and propagating toward the two crack ends. The fracture surface also revealed grainy features adjacent to the ID of the tube.

Both tubes A and B images with the locations for circumference measurements and wall thickness are shown in Figure 9. A dimensional check was conducted to measure the circumference and wall thickness of the two cut-out tubes. Pi-tape measurements were taken at, adjacent to and away from the cracks. Table 3 represents the circumference measurements on both tubes (Tubes A and B) at different locations. It was found that the circumference of Tube A increased at locations D, E and F, which are associated with bulging events. This tube A had swelled with an increase of about 1.03% in circumference at the crack area, as compared to the intact region, which was located away from the crack. The thickness measurements were taken at the sections adjacent to the ends of the tube samples using a point vernier caliper. The measurement results along the selected locations and wall thickness values are shown in Table 4. The thickness of the crack mouth was also reduced as compared to the intact areas due to the increase in circumference. Tube B showed no significant variation in its circumference and thickness at and away from the crack area.

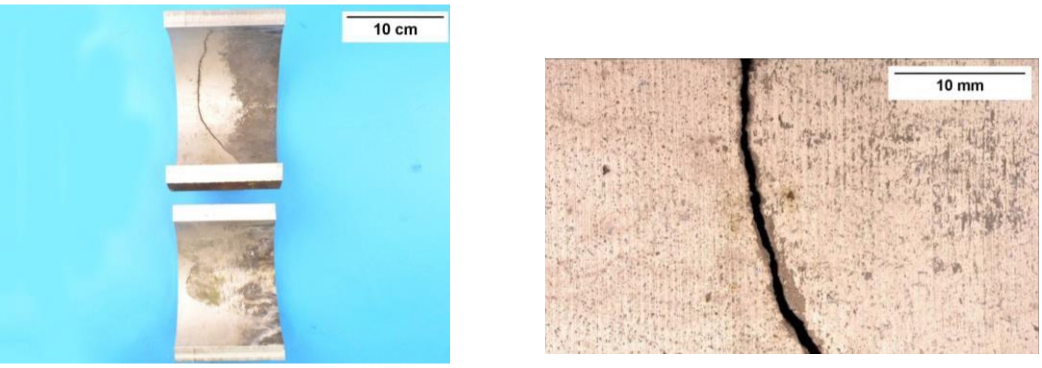

(a) (b)

Figure 7. (a) General view of ID surface and (b) Close-up view of ID surface of rupture in tube B.

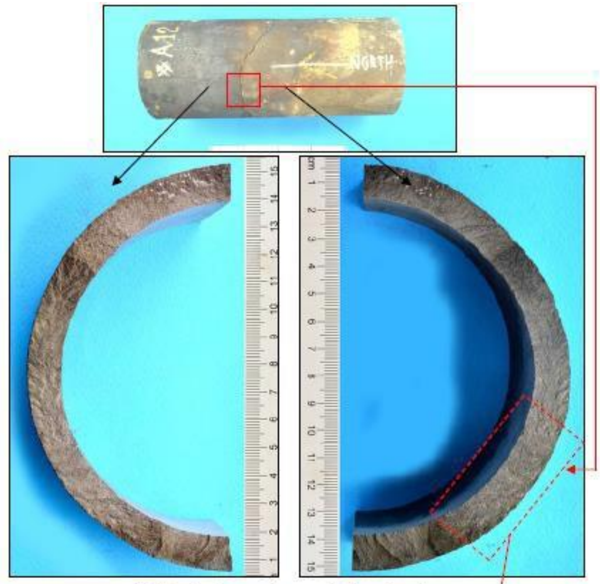

Mating fracture surfaces - Before cleaning

Fracture surface at initiation area- after cleaning

Figure 8. Tube B – Fracture Surfaces; before and after cleaning.

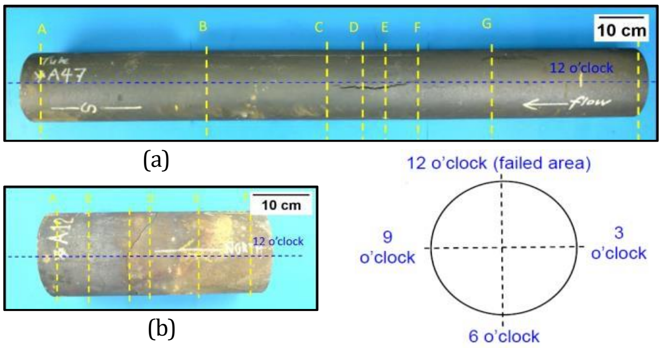

(a)

(b)

Figure 9. The two tubes with the locations for circumference measurements and wall thickness, (a) Tube A and (b) Tube B.

Table 3 Results of the measurement along the selected locations for circumference measurements on both tubes

Parameter	Location	Tube A	Tube B
Circumference (mm)	A	481.3	481.4
	B	482.4	481.3
	C	482.5	481.6
	D	484.2	481.8
	E	486.3	481.5
	F	484.2	481.1
	G	482.2	-
	H	481.3	-

Table 4 Results of the measurement along the selected locations for wall thickness on both tubes

Parameter		Wall Thickness (mm)			
Position		12 o'clock (crack)	3 o'clock	6 o'clock	9 o'clock
Tube A	Location D (crack area)	12.72	12.95	13.13	12.82
	Location A (intact area)	12.71	13.1	13.5	13.43
Tube B	Location C (crack area)	13.6	13.74	13.65	13.6
	Location A (intact area)	13.61	13.74	13.74	13.57

3.3 Energy Dispersive X-ray (EDX) Analysis

The EDX results on the base metal, fracture, ID and OD surfaces of tubes A and B are tabulated in Table 5. In general, tube A revealed the existence of oxygen, chromium, nickel, aluminium, carbon, magnesium, silicon, manganese and iron (Figure 12). While the EDX results on the base metal, fracture, ID and OD surfaces of tube B generally revealed the presence of oxygen, chromium, nickel, aluminium, iron, carbon, magnesium, silicon, manganese and calcium (Figure 13). The elemental contents were essentially associated with oxidation products of the base metal accompanied by some contaminations from the exposed environment. The magnesium, aluminium and carbon contents were likely associated with the catalyst and service medium of the tubes. No significant presence of corrosive species was detected on both tubes A and B.

Table 5 EDX results of both tubes A and B

EDX Mapping Area	Elemental Composition/ Tube	
	Tube A	**Tube B**
Fracture surface	Oxygen, chromium, nickel, aluminium, carbon, silicon, magnesium, manganese	Oxygen, chromium, nickel, aluminium, carbon, magnesium, silicon, manganese, iron
ID surface	Oxygen, chromium, nickel, aluminium, carbon, silicon, magnesium, manganese	Oxygen, chromium, nickel, iron, carbon, magnesium, aluminium, silicon, calcium, manganese
OD surface	Oxygen, chromium, carbon, silicon, aluminium, manganese, iron, nickel	Oxygen, chromium, nickel, iron, aluminium, carbon, magnesium, silicon, calcium, manganese
Base metal	Chromium, nickel, iron, carbon, silicon, manganese, niobium	Chromium, nickel, iron, carbon, silicon, manganese, niobium

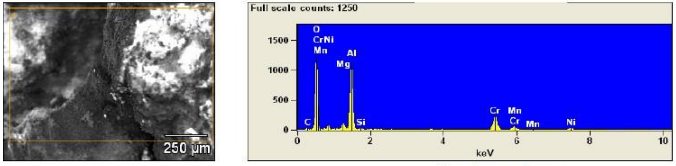

Fracture surface

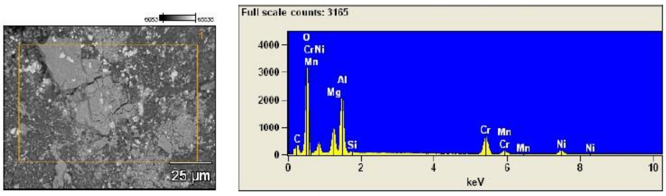

ID surface

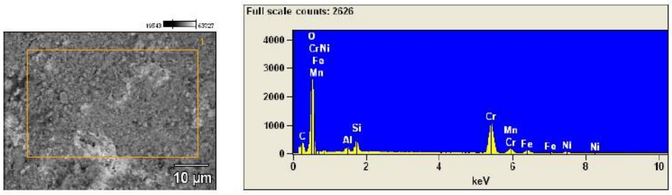

OD surface

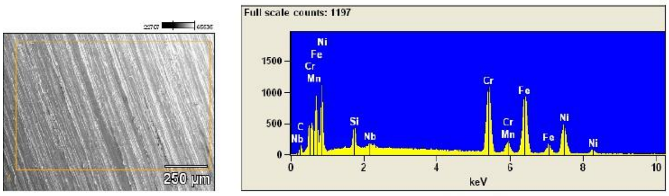

Base metal

Figure 12. The EDX results on the fracture, ID and OD surfaces, and base metal of tube A.

3.4 Sectional Metallography

Sectional metallographic examination was conducted transversely across the following locations of the two cut-out tubes. Figures 14 and 15 display the macrographs and micrographs of tube A. In ruptured section #A, creep voids were observed along the rupture surface (Figure 14). The rupture surface was covered with an oxide scale due to post-rupture exposure to the high-temperature service environment. Numerous sub-surface fissures at the ID, formed by aligned and linked creep voids were observed (Figure 14). The failure of the tube was consistent with creep rupture from the ID. Slight oxidation was observed at the OD and ID surfaces. There was no significant presence of creep voids observed in the reference intact section.

Microstructural analysis of a catalyst tube rupture in a reformer revealed the presence of extensive creep voids along the rupture surface. These creep voids, also known as creep cavities, are indicative of long-term deformation and damage due to the sustained high-temperature and mechanical stresses experienced during the tube's service life. Such observations align with the phenomenon of creep, which is the time-dependent deformation of materials under constant load and elevated temperatures. The formation of these voids can be attributed to the diffusion and coalescence of dislocations and grain boundary sliding, processes typical of materials undergoing creep [12]. This microstructural evidence underscores the importance of carefully controlling the operating conditions and material selection in industrial applications to mitigate the detrimental effects of creep, ensuring the safety and longevity of critical equipment in processes like catalytic reforming.

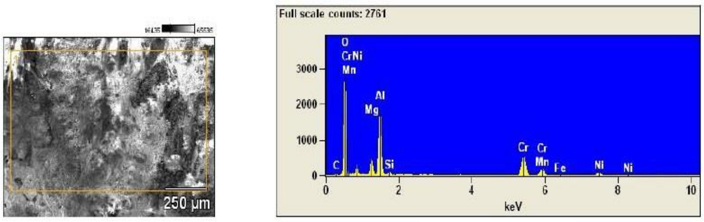

Fracture surface

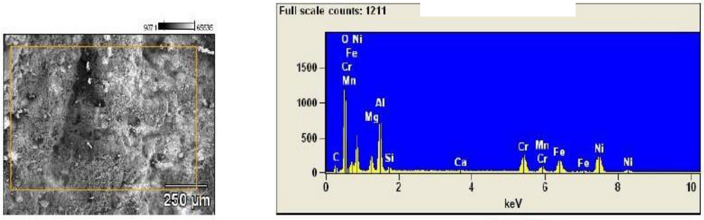

ID surface

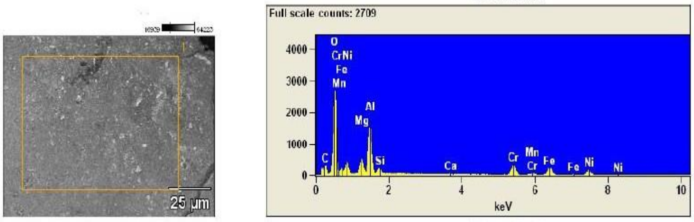

OD surface

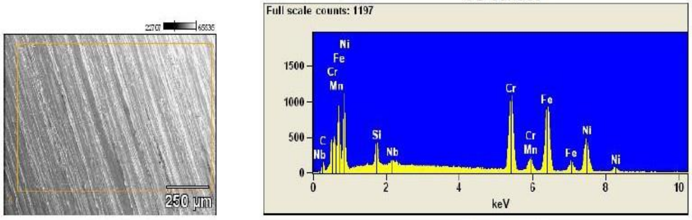

Base metal

Figure 13. The EDX results on the fracture, ID and OD surfaces, and base metal of tube B.

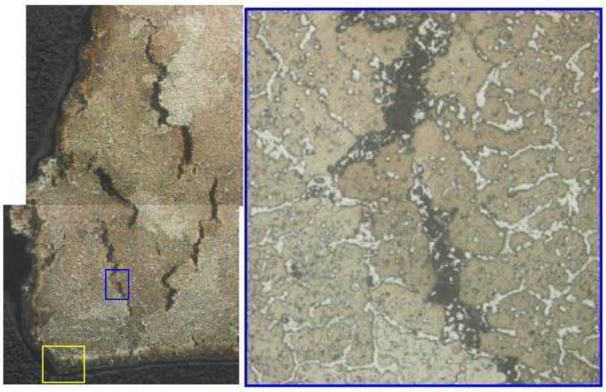

Micrographs at 25x (left) and 200x (right)

Micrograph at 200

Figure 14. Metallographic Section of Tube A (Section #A) – Across Rupture Mouth (ID).

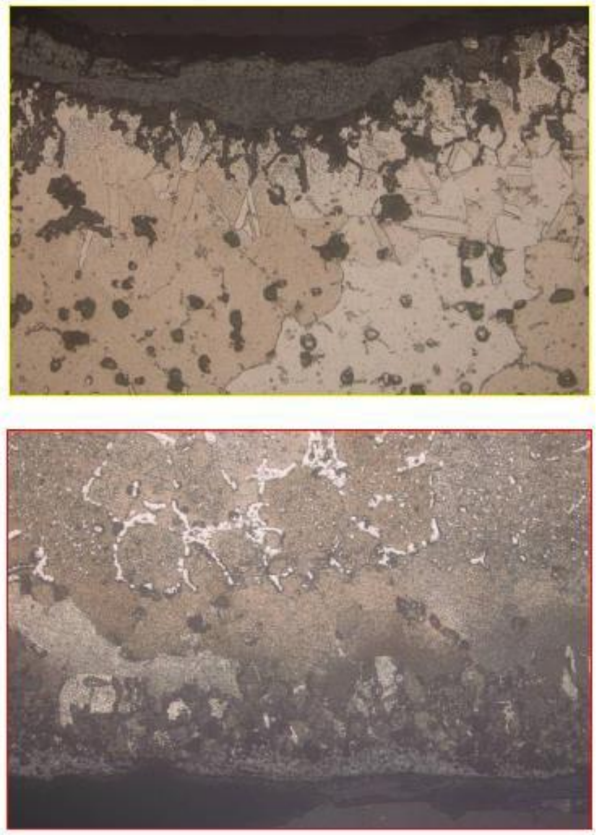

Micrographs of OD (top) and ID (bottom) at 200x

Figure 15. Metallographic Section of Tube A (Section #B) - Across Intact Area.

The macrographs and micrographs of the examined section on tube B are shown in Figures 16, 17 and 18. In section #C1 (across the middle of the crack), it was observed that the crack path across the tube thickness was generally straight apart from a slightly jagged morphology near the OD, resembling intergranular crack propagation from the OD in Figure 16. There was also a similar intergranular incipient crack propagation from the OD adjacent to the through-thickness crack, as shown in Figures 16 and 17.

The crack propagation towards the crack end in section #C2 (Figure 18) was generally transgranular in nature. The exposed surface along the crack length had generally been oxidised due to post-fracture exposure. A slight extent of creep voids was observed along the crack, likely due to the cracked tube's reduced strength capacity as seen in Figure 18. The crack initiation of the tube appeared to be associated with embrittlement, likely due to thermal shock failure. The subsequent crack propagation was consistent with the creep-fatigue cracking mechanism. Slight oxidation was observed at the OD and ID surfaces. The condition of the reference section was generally satisfactory with no presence of cracks.

Upon exposure to high temperatures during service, the cast microstructure of the reformer tube material experiences alterations in carbide morphology. It is noteworthy that the exposure temperature plays a more significant role in inducing these microstructural changes than the duration of exposure [13]. The damage associated with creep in reformer tubes manifests as aligned voids and multiple cracks. The coarsening of both primary and secondary carbides provides clear evidence of ageing, particularly in high-temperature conditions [14]. These radiant tubes are subjected to both sustained high temperatures and cyclic mechanical stresses which are coherent with the creep-fatigue cracking. These two stressors act synergistically, exacerbating the crack formation and propagation rate. The elevated temperatures cause the material to creep, developing creep voids or cavities within the microstructure. These voids are stress concentrators, making the material more susceptible to fatigue cracking. The cyclic mechanical loading then induces crack initiation and growth, further weakening the material.

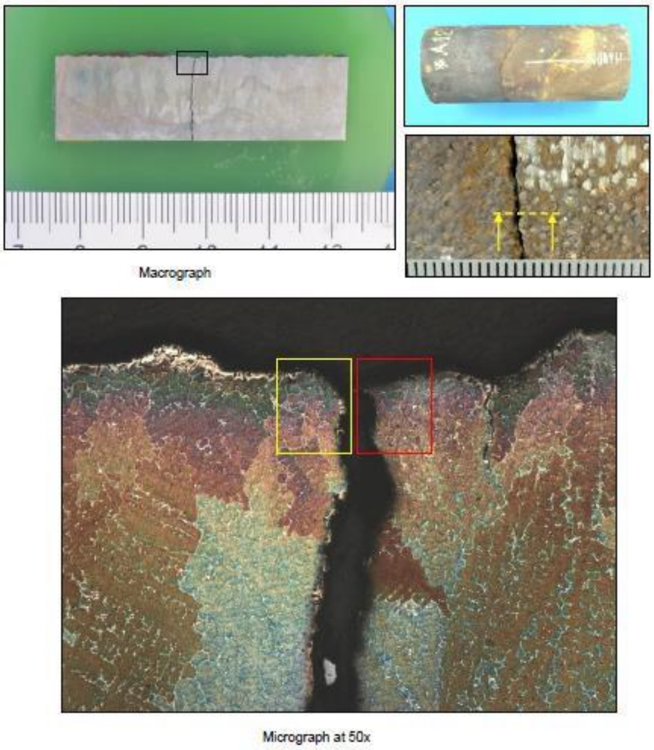

Figure 16. Metallographic Section of Tube B (Section #C1) — Across Middle of Crack Length. It was observed that the crack path across the tube thickness was generally straight apart from a slightly jagged morphology near the OD, resembling intergranular crack propagation from the OD.

Notably, these creep voids are isolated in nature, and post-service annealing procedures have been observed to enhance carbide morphology [13]. These observations raise the possibility of a considerable remaining creep life in the material. This work supports the damage caused by the premature failure of reformer tubes' hot section parts, including creep of the tube material, thermal shock, overheating, and carburization of the inner wall [13, 15].

3.5 Vickers Micro-hardness Test

The Vickers micro-hardness test was carried out in accordance with ASTM E384-22 standard [9]. The micro-hardness test results in Vickers hardness number (HV) are shown in Table 6. The examined locations of tube A had average hardness values in the range of 181 up to 200 HV, whilst tube B had an average hardness in the range of

222 up to 228 HV. The lower hardness values of tube A were possibly due to a decrease in hardness as a result of stress relaxation during the creep failure. The increasing hardness value on Tube B was possibly due to carbide precipitation along the grain boundary.


Micrograph at 200x

Figure 17. Metallographic Section of Tube B (Section #C1) —Across Middle of Crack Length.

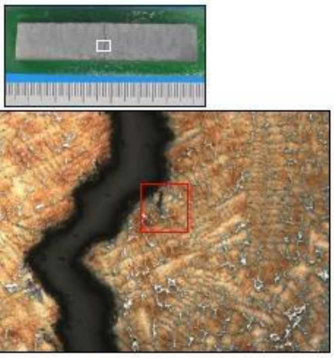
Micrograph at 50x

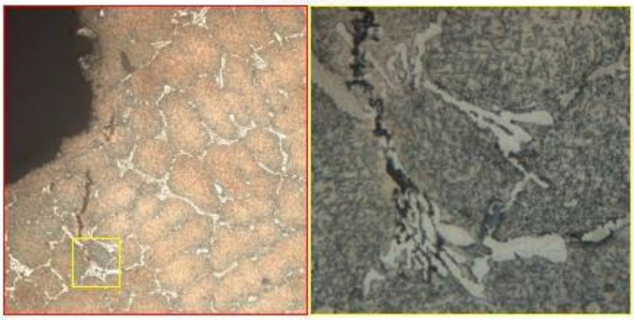
Micrographs at 200x (left) and 1000x (right)

Figure 18. Metallographic Section of Tube B (Section #C2) — Across Crack End. The crack propagation towards the crack end was generally transgranular.

Table 6 Vickers micro-hardness results for both tubes A and B

Location			Micro- Hardness Values (HV)	Standard Deviation (in %)
Tube A Section #A	Rupture area	Adjacent ID surface	196	1.93
		Adjacent OD surface	196	5.60
Tube A Section #B	Base metal area		202	3.69
Tube B Section #C	Crack area	Adjacent ID surface	228	2.47
		Adjacent OD surface	226	2.92
Tube B Section #D	Base metal area		229	3.52

3.6 Tensile Test

The tensile strength of both tubes generally complied with the tensile requirements of H39WM alloy steel material, which required a minimum strength of 450 N/mm^2. This data can be viewed in Table 7. It was shown that the tensile strength of tube A was lowered compared to tube B, which was possibly due to stress relaxation during the creep failure. The material has softened due to prolonged service exposure, which is also apparent from the presence of coarse carbides at dendritic boundaries and the disappearance of fine intra-dendritic precipitation [16].

Table 7 Tensile test results for tubes A and B

Parameter	Tube A	Tube B
Measured Diameter (mm)	8.84	8.77
Effective Area (mm^2)	51.38	62.35
Yield Load (kN)	12.33	20.08
Yield Stress (N/mm^2)	240	322
Ultimate Tensile Load (kN)	27.6	34.7
Ultimate Tensile Strength (N/mm^2)	450	557
Gauge Length (mm)	35	35
Elongation (%)	9	7
Reduction of Area (%)	4	6

3.7 Related Mechanisms

Creep rupture is a distinctive failure mechanism that occurs when materials are exposed to prolonged high temperatures and sustained mechanical stress. It is characterised by the slow and time-dependent deformation of the material, typically encountered in conditions where the temperature is significantly below the material's melting point but still elevated. The primary mechanism underlying creep rupture involves the movement of dislocations within the crystalline structure of the material. As mechanical stress persists, these dislocations slowly traverse the material's lattice, resulting in a gradual, continuous deformation. Over time, this deformation accumulates, leading to the development of microscopic voids or cavities within the material. These voids act as stress concentrators, making the material increasingly susceptible to rupture. The presence of bulging is a clear indicator of this process. When the mechanical stress and temperature conditions surpass a critical threshold, the material reaches its breaking point, and the accumulated deformation culminates in the failure of the component, which is evident through the characteristic bulging. Creep rupture is particularly relevant in applications where materials are exposed to extended periods of elevated temperature and mechanical loads, such as in power plants and petrochemical industries. Managing and understanding this mechanism is essential to ensure the safety and integrity of these critical components.

Creep-fatigue cracking, induced by thermal shock, is a complex failure mechanism that results from the simultaneous effects of two primary modes of material degradation: creep and fatigue. Thermal shock occurs when a material experiences rapid and extreme temperature changes, causing it to expand and contract rapidly. This thermal cycling leads to stress variations within the material. Creep, on the other hand, is the time-dependent deformation of materials under sustained mechanical loads and elevated temperatures. When subjected to thermal shock, materials undergo cyclic thermal expansion and contraction, generating internal stresses. These rapid changes in temperature and the associated mechanical stress fluctuations can create microstructural flaws or initiate cracks within the material. As a result, the material experiences both creep deformation and fatigue-related crack propagation simultaneously. The cumulative effect of these two processes ultimately leads to creep-fatigue cracking. This phenomenon is especially relevant in situations where components are exposed to sudden temperature changes. Understanding and managing it is critical for ensuring the durability and safety of such components. Strategies to mitigate creep-fatigue cracking due to thermal shock may include material selection, design considerations, and operational practices that minimize extreme temperature fluctuations.

Additionally, understanding the damage mechanisms, such as creep rupture and fatigue cracking, is vital for developing targeted preventive actions.

3.8 Preventive Actions

It is crucial to take proactive measures to ensure the efficiency and dependability of catalyst tubes in a steam reforming unit. This helps in detecting and resolving potential problems proactively, thus averting tube failures and unplanned shutdowns. Proactive measures may involve:

a) Regular Inspection and Testing
Conduct visual inspections of the catalyst tubes during in-service to detect early signs of damage such as physical tube changes / abnormal tube appearance such as bowing, hot- banding, speckling, giraffe-necking etc. Periodical Tube Metal Temperature (TMT) measurement to detect hotspots at tube skin. Offline robotic tube inspection crawler to measure OD growth and defects. During plant shutdown orturnaround opportunity, the catalyst level shall be measured for suspected catalyst breakages.

b) Root Cause Analysis
Conduct a thorough root cause analysis for any tube failures that occur. Understanding the specific mechanisms of failure will enable more targeted and effective preventive actions.

c) Documentation and Reporting
Maintain comprehensive records of all maintenance activities, inspections, and incidents related to the catalyst tubes. Regularly review this data to identify trends and patterns that can inform future preventive measures.

d) Continuous Improvement
Foster a culture of continuous improvement where lessons learned from each incident or inspection are applied to enhance the reliability and safety of the catalyst tubes and the steam reforming process as a whole.

e) Operational Parameters
Review and optimize operational parameters such as temperature, pressure, and flow rates to ensure they fall within safe and stable ranges. Modifications to operating conditions can help reduce thermal stress and extend tube life.

With these preventive measures, the risk of catastrophic tube failures can be reduced, the lifespan of their catalyst tubes can be prolonged and production of hydrogen and synthesis gas in the steam reforming unit can be sustained consistently. These measures contribute to a safer, more efficient, and environmentally responsible industrial operation.

4. CONCLUSIONS

In conclusion, the failure of tube A revealed a form of damage known as creep rupture, which was evidenced by the presence of bulging and extensive presence of creep voids and fissures in the locally affected area of the tube. This bulging indicates that the tube experienced time-dependent deformation at elevated temperatures, leading to the development of internal stress and ultimately the rupture of the tube. Creep rupture is a common mode of failure in materials subjected to sustained high temperatures and mechanical stress, and the observation of bulging is a clear indicator of this damage mechanism.

However, the failure on tube B was primarily attributed to intergranular crack initiation at the OD surface. This was likely due to thermal shock cracking, which is when rapid temperature changes cause stress and lead to cracks between grain boundaries. The subsequent crack propagation within the tube was primarily driven by a fatigue mechanism, indicating that the ongoing cyclic loading and unloading caused the cracks to grow, eventually leading to the tube's failure.

This comparative analysis of creep rupture and thermal This comparative analysis of creep rupture and thermal shock failures in nickel-based alloy reformer tubes has been successfully discussed. By contrasting these two mechanisms, the study underscores the importance of tailored operational practices to mitigate each type of failure. Future research should further explore material improvements and optimised operating conditions to address these high-temperature challenges.

ACKNOWLEDGEMENTS

The author would like to express gratitude and appreciation to the technical support from our industry partner (which has to undisclosed their names) and academic support from the Faculty of Chemical Engineering and Technology, Universiti Malaysia Perlis (UniMAP), for their involvement in the research. This research was funded and supported under grant number FRGS/1/2020/STG05/UNIMAP/02/3 by the Fundamental Research Grant Scheme (FRGS) from the Ministry of Education Malaysia.

REFERENCES

[1] Abbas Bahrami and Peyman Taheri (2019). Creep Failure of Reformer Tubes in a Petrochemical Plant, Metals, 9, 1026.

[2] Padma Kodali and John P. Richert (2003). Failure Mechanisms of Alloy 800H in Steam Reformer Furnace Pigtails in NACE Corrosion 2003**,** San Diego, California.

[3] Heloisa Cunha Furtado and Iain Le Mayb (2004). High-Temperature Degradation in Power Plants and Refineries, Materials Research, Vol. 7, No. 1,1 103-110.

[4] Erik A. A. Nilsson, “Degradation Mechanisms of Heat Resistant Steel at Elevated Temperatures in an Iron Ore Pelletizing Industry”, Doctoral Thesis, Division of Material Science, Department of Engineering Sciences and Mathematics, Luleå University of Technology, 2017.

[5] A. K. Ray, S. Kumar, G. Krishna, M. Gunjan, B. Goswami, and S. C. Bose, "Microstructural Studies and Remnant Life Assessment of Eleven Years Service Exposed Reformer Tube," Materials Science and Engineering A, vol. 529, pp. 102-112, 2011.

[6] ASTM. "ASTM E415-17: Standard Test Method for Analysis of Carbon and Low-Alloy Steel by Spark Atomic Emission Spectrometry." ASTM International, 2017.

[7] ASTM. "ASTM E3-11 (Ra 2017): Standard Guide for Preparation of Metallographic Specimens." ASTM International, 2017.

[8] ASTM. "ASTM E407-07 (Ra 2015): Standard Practice for Microetching Metals and Alloys." ASTM International, 2015.

[9] ASTM. "ASTM E384-22: Standard Test Method for Microindentation Hardness Of Materials." ASTM International, 2022.

[10] ASTM. "ASTM E8/E8M-22: Standard Test Methods for Tension Testing of Metallic Materials." ASTM International, 2022.

[11] Alloy Digest, Paralloy H39WM (Cast heat resisting austenitic alloy (Microalloyed)), Alloy Digest, 44 (5): SS-594, 1995.

[12] M. Mudang, E. Hamzah, H. R. Bakhsheshi-Rad, and F. Berto, “Effect of Heat Treatment on Microstructure and Creep Behavior of Fe-40Ni-24Cr Alloy,” Applied Sciences, vol. 11, no. 17, p. 7951, Aug. 2021, doi: 10.3390/app11177951.

[13] J. Swaminathan, R. Singh, S. K. Das, and G. Das, "Failure Analysis of Welded Reformer Tubes of a Fertilizer Unit," in Proceedings of the International Conference & Exhibition on Pressure Vessels and Piping, "OPE 2006 – CHENNAI," Chennai, India, 7-9 February 2006.

[14] X. Xiang, Z. Yao, J. Dong, and L. Sun, "Dissolution behavior of intragranular M23C6 carbide in 617B Ni-base superalloy during long-term aging," *J. Alloys Compd.*, vol. 787, pp. 216-228, May 2019.

[15] A. K. Ray, S. K. Sinha, Y. N. Tiwari, J. Swaminathan, G. Das, S. Chaudhuri, and R. Singh, "Analysis of Failed Reformer Tubes," Engineering Failure Analysis, vol. 10, pp. 351-362, 2003.

[16] A. Raj, N. Roy, B.N. Roy, and A.K. Ray, "Life Estimation and Creep Damage Quantification of Service Exposed Reformer Tube," High-Temperature Materials and Processes, vol. 34, no. 7, pp. 731-742, 2015.